Systematic analysis of porosities in metal-organic frameworks

Kai Trepte[1, a)] and Sebastian Schwalbe[2]
[1)] *SUNCAT Center for Interface Science and Catalysis, SLAC National Accelerator Laboratory, 2575 Sand Hill Road, Menlo Park, California 94025, USA*
[2)] *Institute of Theoretical Physics, TU Bergakademie Freiberg, Leipziger Str. 23, D-09596 Freiberg, Germany*

(Dated: 5 August 2020)

Accurate numerical calculations of porosities and related properties are of importance when analyzing metal-organic frameworks (MOFs). We present `porE`, an open-source, general-purpose implementation to compute such properties and discuss all results regarding their sensitivity to numerical parameters. Our code combines the numerical efficiency of FORTRAN with a user-friendly PYTHON interface. Two different approaches to calculate porosities are implemented in `porE`, and their advantages and drawbacks are discussed. In addition to this functionality, `porE` can calculate pore size distributions and offers the possibility to analyze pore windows. The underlying approaches are outlined. Pore windows are discussed concerning their impact on the analyzed porosities. Comparisons with experimental values aim for a clear differentiation between void and accessible porosities, which we provide. This work highlights that the calculated quantities are sensitive to the choice of numerical parameters and that a careful evaluation of convergence is essential.

I. INTRODUCTION

Metal-organic frameworks (MOFs) are a material class aiming for different possible applications[1], such as gas absorbers[2,3], catalysts[4–6], optical sensors[7,8], and post-synthetic modification (PSM) of MOFs for modulating reaction outcomes and biomedical applications[9]. The class of amorphous MOFs (aMOFs) has possible applications as liquids or melt quenched glasses[10]. Recently, it has been shown that the pore sizes in MOFs can be varied by enforcing an external pressure on a given MOF[11]. Many applications of MOFs are based on the porous nature of these materials, as MOFs typically exhibit several pores. These pores usually have different sizes. With that, an accurate determination of the porosity and the pore sizes is important[12].

In general, the porosity Φ is defined as the empty volume V_{empty} within a given total volume V_{total}, e.g., the unit cell of a MOF.

$$\Phi = \frac{V_{\text{empty}}}{V_{\text{total}}}. \tag{1}$$

While the total volume for crystal structures is always well defined, the empty volume misses this general definition. One major aim of this work is to define and clearly separate two different empty volumes, namely the void volume V_{void} and the accessible volume V_{acc}. The void volume is the space that is not occupied by any atom in the unit cell. This volume can easily be analyzed given the sizes of the atoms, e.g., their respective van der Waals (vdW) radii[13]. With this volume, the void porosity Φ_{void} can be obtained, which serves as a first descriptor of a porous material. However, it has to be considered that a void porosity does not necessarily reflect the volume/porosity which can be assumed by adsorbed species. Such a porosity strictly depends on the size of that species. With that, another volume occurs, i.e., the accessible volume. Accordingly, the accessible porosity Φ_{acc} can be defined. This porosity, in contrast to Φ_{void}, depends on a probe radius r_{probe} which varies for different species. One has to be careful when analyzing the porosity in a material, as the porosity of interest is usually Φ_{acc}. When reporting this quantity, one needs to provide the respective probe radius, such as the vdW radius of H ($r_{\text{probe}} = 1.20$ Å) or Xe ($r_{\text{probe}} = 2.16$ Å).

Within this work it will be shown that choosing different probe radii significantly impacts the evaluated porosity. A systematic analysis of the probe radius dependence allows to evaluate the porosity for any adsorbed species, i.e., any atom or molecule with an effective probe radius. Furthermore, additional details about the underlying MOF (i.e., pore sizes) are automatically obtained when carrying out such a systematic study.

This manuscript is structured as follows: in the next section, the theoretical background as well as detailed aspects of the implementation for the different approaches - an overlapping spheres approach (OSA) and a grid point approach (GPA) - are presented, including discussions about the grid size dependence for the GPA as well as the importance of the probe radius dependence for the accessible porosity. Afterwards, an ansatz to calculate the pore size distribution is outlined, following by an approach to determine pore windows. A comparison to reference values comes right before the conclusion.

II. THEORETICAL BACKGROUND

We developed the `porE` code to analyze the porosities and related properties numerically. While numerical demanding routines are written in FORTRAN, these routines are available through a PYTHON user-interface. Thus, our `porE` code combines numerical efficiency with

[a)] Electronic mail: ktrepte@stanford.edu or kai.trepte1987@gmail.com

user-friendliness. The open-source `porE` code, under licence Apache 2.0, is available at github, i.e., `https://github.com/kaitrepte/porE`, and can easily be installed through the PYTHON pip package manager. For calculations using `porE`, one only needs the unit cell parameters and the coordinates of the atoms as input, similar to alternative implementations[14–18]. Two different approaches are implemented, namely an overlapping spheres approach (OSA) and a grid point approach (GPA). While the OSA is very fast and gives a good approximation for the (void) porosity, the GPA is able to distinguish between void and accessible properties and can be tuned to any desired accuracy. Both approaches are summarized below. Further, `porE` can calculate the pore size distribution (PSD) and, based on PSD results, allows for an evaluation of pore windows. These options are described below as well.

For this study, the MOFs UiO-66[19–21], UiO-67[20–22], DUT-8(Ni)$_{\text{open}}$[23–25], DUT-8(Ni)$_{\text{closed}}$[23], IRMOF-10[26], MOF-5[27], HKUST-1[28–30] and MOF-210[31] are investigated. For convenience, the two structures (open, closed) of DUT-8(Ni) are abbreviated with DUT-8(Ni)$_{\text{o}}$ and DUT-8(Ni)$_{\text{c}}$. Further, MOF-210 is only analyzed with the OSA, as its structure is currently to large to be properly analyzed with the GPA.

For illustration, pore centers determined using `porE` are plotted as spheres within the periodic structures of the investigated MOFs (see Fig. 1).

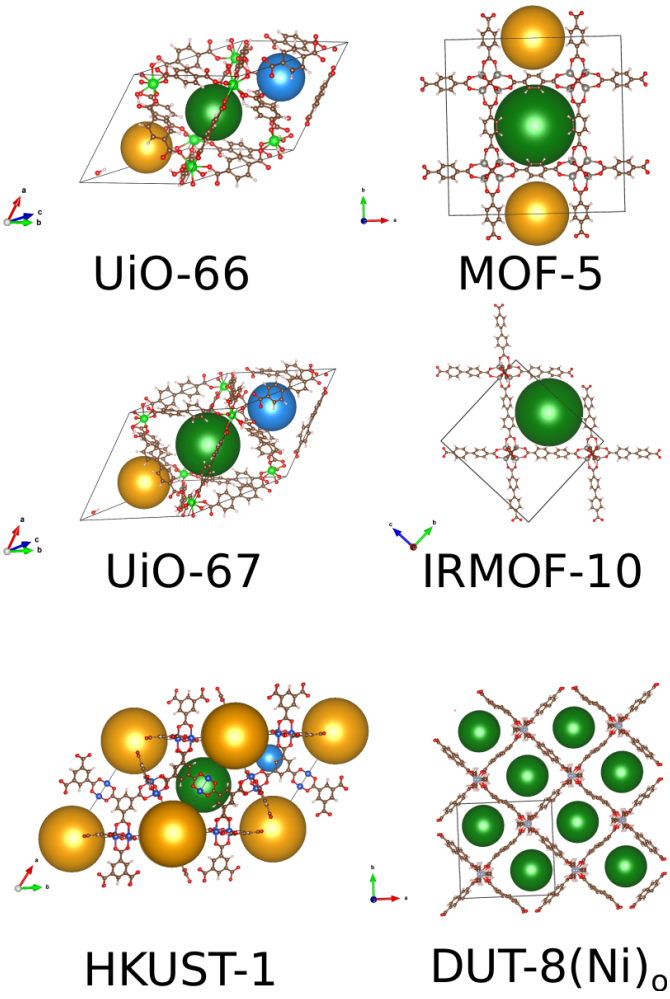

FIG. 1. Pores visualized as spheres for the test set of MOFs. HKUST-1, UiO-66, and UiO-67 have three distinct pores. MOF-5 has two characteristic pores, while DUT-8(Ni)$_{\text{o}}$ and IRMOF-10 have one pore, which is repeated within the periodic structure. The individual pictures are generated with VESTA using the calculated pore centers as additional species with an effective radius equal to the determined pore size. The entire picture was generated using the INKSCAPE program.

A. Overlapping sphere approach (OSA)

To evaluate the porosity within MOFs (or any porous material), a hard sphere model can be used. In such a model, the overlap of atomic spheres is evaluated and consequently subtracted from the total volume of all spheres/atoms. The volume which is left, V_{void}, can be compared to the total volume of a unit cell, providing the (void) porosity Φ_{void} as

$$\Phi_{\text{void}} = \frac{V_{\text{void}}}{V_{\text{total}}}, \tag{2}$$

with the void, total, occupied, atomic and overlap volumes given by

$$V_{\text{void}} = V_{\text{total}} - V_{\text{occ}} \tag{3}$$
$$V_{\text{total}} = \mathbf{a} \cdot (\mathbf{b} \times \mathbf{c}) \tag{4}$$
$$V_{\text{occ}} = V_{\text{atoms}} - V_{\text{overlap}} \tag{5}$$
$$V_{\text{atoms}} = \sum_i V_{i,\text{vdW}} \tag{6}$$
$$V_{\text{overlap}} = \sum_{i,j>i} V_{ij,\text{overlap}}. \tag{7}$$

Here, $\mathbf{a}$, $\mathbf{b}$ and $\mathbf{c}$ are the unit cell vectors and $V_{i,\text{vdW}}$ is the volume of a sphere with a radius equal to the vdW radius of atom i. The sum of the volumes of all atoms V_{atoms} minus the overlap V_{overlap} between pairs of atoms defines the occupied volume V_{occ}. The overlap volume can be calculated analytically following the derivation in the supplemental material. This is done if the sum of the covalent radii is smaller than the distance between atoms i and j, thus if $r_i^{\text{covalent}} + r_j^{\text{covalent}} \leq d_{ij}$. This simple approach gives reasonable results (see Tab. I, a comparison to literature values is given in Tab. VI) at essentially no computational cost.

As higher-order terms are neglected, only the two-center overlap is calculated. However, the OSA recovers the total overlap (three-order and higher terms) almost entirely for the benzene molecule. The literature value[32] of the occupied volume in benzene, treating only the C-C overlap, is $V_{\text{occ}}^{\text{ref}} = 114.8$ Å^3. The proposed OSA delivers a value of $V_{\text{occ}}^{\text{OSA}} = 115.2$ Å^3. For comparison, the

TABLE I. All volumes V (in Å^3) for the determination of the porosity Φ (in %) of all considered MOFs based on the simple overlapping sphere approach (OSA).

MOF	V_{total}	V_{atoms}	V_{overlap}	V_{occ}	V_{void}	Φ_{void}
DUT-8(Ni)$_{\text{o}}$	3190	1953	709	1244	1946	61
DUT-8(Ni)$_{\text{c}}$	648	976	324	652	−4	−1
UiO-66	2308	1992	823	1169	1139	49
UiO-67	4972	2906	1308	1599	3374	68
IRMOF-10	10099	2549	1297	1252	8847	88
MOF-5	17305	6536	2592	3944	13362	77
HKUST-1	4546	2499	1062	1437	3109	68
MOF-210	144400	29385	14937	14449	129952	90

sum of the vdW spheres of all atoms is 166.9 Å^3. The molecular geometry is taken from the CCCBDB[33] with $d_{\text{C-C}} = 1.397$ Å, in analogy to Gibson and Scheraga [32]. Given this result, it can be assumed that the results for the overlap should be accurate, even without the higher-order terms.

The main advantage of the OSA is the access of reasonable results with essentially no numerical effort. For example, the calculation for MOF-210 (1854 atoms per unit cell) takes about 1 s (see supplemental material). The main disadvantage is that technically only the void porosity is calculated and there is no information about accessible terms. The approach presented in the next section overcomes this shortcoming.

B. Grid point approach (GPA)

An alternative approach to calculate the porosity is based on a numerical grid inside the unit cell. This procedures requires the explicit treatment of each grid point. Any grid point is either close to an atom (inside its vdW sphere) and can be considered occupied. If no such occupation is found, the grid point is considered unoccupied. In analogy to equation (2), the void porosity can be evaluated by the number of unoccupied points divided by the total number of grid points

$$\Phi_{\text{void}} = \frac{N_{\text{unoccupied}}}{N_{\text{total}}}. \tag{8}$$

A suitable amount of grid points will provide accurate results. Using this ansatz, one obtains an insight into the void volume and thus the void porosity. This is not equivalent to the accessible volume and porosity, which is often given in the literature. Thus, one needs to be careful when comparing, e.g., the values for DUT-8(Ni)$_{\text{closed}}$ as explained in the supplemental material.

The accessible volume can be obtained by modifications to the presented ansatz. Grid points need to be evaluated such that around each grid point, a sphere with a probe radius r_{probe} is assumed. If this sphere has no contact with the vdW surface of the MOF, all points inside this sphere are considered to be unoccupied as well as accessible. With that, points can be occupied, unoccupied and not accessible or unoccupied and accessible (see Fig. 2). This ansatz gives rise to another quantity, the accessible porosity Φ_{acc}, which depends on the probe radius $\Phi_{\text{acc}} = \Phi_{\text{acc}}(r_{\text{probe}})$. The relation $\Phi_{\text{acc}}(r_{\text{probe}}) \leq \Phi_{\text{void}}$ is clearly fulfilled. The basic outline of the procedure is given in Fig. 3.

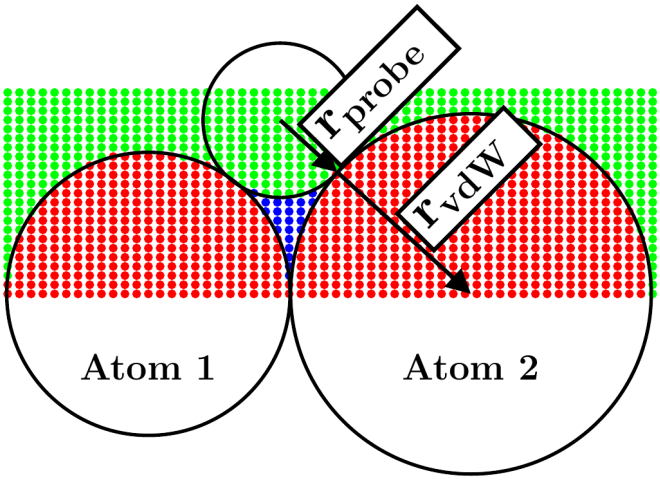

FIG. 2. Visual explanation of different grid points in the GPA. If a grid point is inside the vdW sphere of an atom, it is occupied (red). Otherwise, it is unoccupied. Then, two different cases can occur. If the point is in a region which can be accessed as described by a given probe radius r_{probe} (green), it is unoccupied and accessible. Otherwise, it is unoccupied and not accessible (blue). The difference in the blue and the green points defines the difference between the void and the accessible porosity.

The used grid is defined either as a total number of grid points for each cell vectors or as an approximate grid density per Å for all cell vectors. In either case, the grid points are placed along the cell vectors. With that, a unique grid for any system is generated. This grid can either be uniform, i.e., grid density along all cell vectors is the same, or non-uniform. In this work, we only investigate uniform grids.

From a numerical point of view, the variable $N_{\text{check\_acc}}$ is introduced (see Fig. 3). With this variable, there is no need to loop over all accessible points to determine which unoccupied points are also accessible. Only selected points have to be evaluated (see Fig. 4). This reduces the computational time while not changing the results. The variable $N_{\text{check\_acc}}$ is defined as a subset of points chosen from all immediately accessible points, i.e., all points with a distance larger than $r_{\text{vdW}} + r_{\text{probe}}$ for all atoms. This subset contains points which have a distance within $r_{\text{vdW}} + \delta$, with $\delta = r_{\text{probe}} \cdot (1.0 + h)$, $h = 1.0/\overline{n}$ and $\overline{n}$ is the average grid point density per Å. Accordingly, δ becomes smaller for larger grids. All points k within this subset are within a distance of $r_{\text{vdW}} + r_{\text{probe}} \leq d_k \leq r_{\text{vdW}} + \delta$. Visually, this subset forms a layer of thickness $\delta - r_{\text{probe}} = r_{\text{probe}} \cdot h = r_{\text{probe}}/\overline{n}$ over

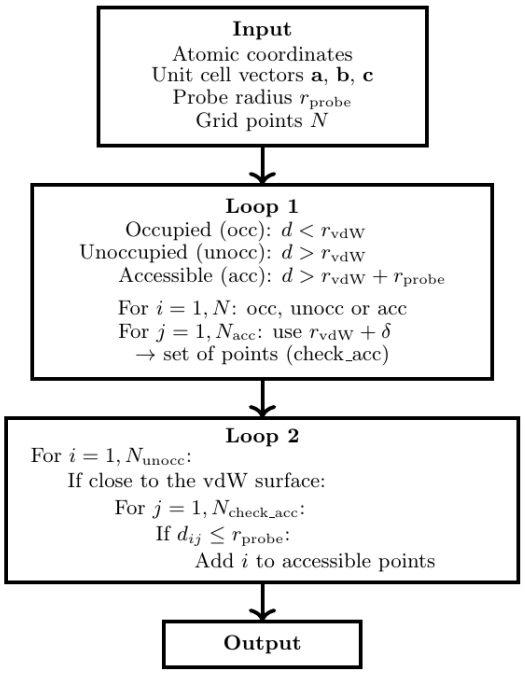

FIG. 3. Outline of the grid point approach (GPA) to evaluate void and accessible porosities (and related properties). In loop 1, everything regarding the void porosity is collected (occupied, unoccupied and all immediately accessible points). During loop 2, it is determined which unoccupied points are also accessible. This ensures that all remaining accessible points are collected for the accessible porosity. Here, $\delta = r_{\mathrm{probe}} \cdot (1.0 + h)$, with $h = 1.0/\overline{n}$ and $\overline{n} = (n_x + n_y + n_z)/3$ being the average grid point density per Å in all directions. Thus, the denser the grid, the smaller δ.

the vdW surface of the MOF (indicated in gray in Fig. 4).

The obtained subset ($N_{\mathrm{check\_acc}}$) is used to identify whether unoccupied points are also accessible. If the distance of any unoccupied point to any point in $N_{\mathrm{check\_acc}}$ is smaller than r_{probe}, the unoccupied point is accessible (green point in Fig. 4). Otherwise, the point is not accessible (blue point in Fig. 4). Further modifications to this approach can be introduced, where $N_{\mathrm{check\_acc}}$ is only obtained per atom. If an unoccupied point is close to an atom i, only the points $N_{\mathrm{check\_acc},i}$ need to be evaluated. This is the basis of $\mathrm{GPA}_{\mathrm{sub\text{-}grid}}$ (see supplemental material), which gives an additional speed-up.

a. Grid size dependence As the GPA depends on the (uniform) distribution of grid points, it is important to determine how dense the grid needs to be to provide numerically reliable results. For all structures (except MOF-210), the grid was successively increased and the porosities (void and accessible) were calculated. A probe radius of 1.20 Å was used for all MOFs. In addition, a probe radius of 2.16 Å has been employed for DUT-8(Ni)$_{\mathrm{open}}$, UiO-66 and UiO-67. This was done to see whether the porosities converge differently using different probe radii. The results for all MOFs are summarized in the supplemental material. For UiO-66, the results are given in Fig. 5.

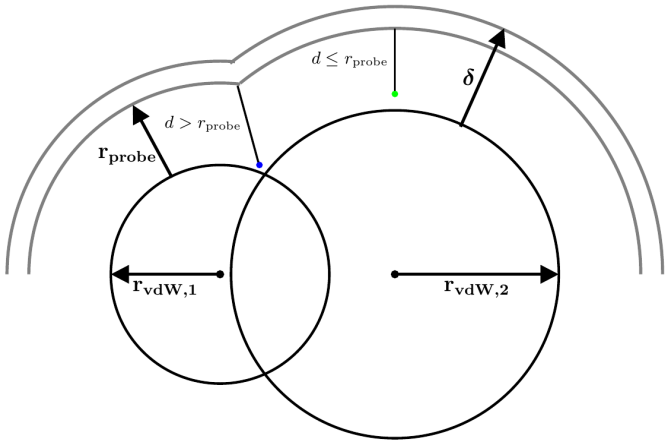

FIG. 4. Visualization of $N_{\mathrm{check\_acc}}$. Circles for Atom 1 and Atom 2 indicate their respective vdW radii r_{vdW}. The subset of points $N_{\mathrm{check\_acc}}$ is chosen from all immediately accessible points, i.e., all points with a distance larger than $r_{\mathrm{vdW}} + r_{\mathrm{probe}}$ for all atoms. This subset (indicated in gray) contains points which have a distance within $r_{\mathrm{vdW}} + \delta$, where $\delta = r_{\mathrm{probe}} \cdot (1.0 + h)$, $h = 1.0/\overline{n}$ and $\overline{n}$ is the average grid point density per Å. Accordingly, δ becomes smaller for larger grids. If the distance of an unoccupied point to any $N_{\mathrm{check\_acc}}$ is smaller than r_{probe}, this point is also accessible (green). Otherwise, it is not accessible (blue, color code adopted from Fig. 2).

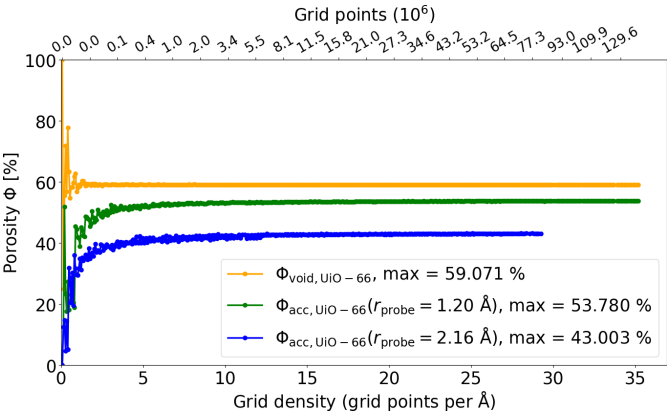

FIG. 5. Grid size dependence for UiO-66. The void porosity as well as the accessible porosity for two different probe radii are shown. The x-axes denote the used grid. Maximum grid: $\approx 35/\text{Å} \rightarrow 1.42 \cdot 10^8$ points for $r_{\mathrm{probe}} = 1.20$ Å and $\approx 29/\text{Å} \rightarrow 8.17 \cdot 10^7$ points for $r_{\mathrm{probe}} = 2.16$ Å.

Clearly, the void porosity converges very fast with an increasing grid, and even a smaller number of grid points provides good results. For the presented example, a grid point density of 5 points/Å seems to be sufficient for the void porosity. On the other hand, the accessible porosity converges much slower, and more grid points are needed to reach convergence. Using our example, at least 10 points/Å are needed to sufficiently converge the results. This is true for the other MOFs as well.

Using different probe radii influences the convergence as well. Furthermore, the accessible porosity for the different probe radii is very different. This will be discussed in the next section in more detail.

b. Probe radius dependence After establishing that a grid size of ca. 10 points/Å is sufficient for an accurate description of the porosities, the next question is how the accessible porosity changes for different probe radii. This becomes especially important if the porosity is analyzed with respect to different adsorbed species, having different effective probe radii. Furthermore, it is important to analyze this behavior regarding the comparison with literature values. Usually, the accessible porosity is reported, while the probe radius is typically disregarded. Here we show that the accessible porosity strongly depends on the probe radius, which can be seen for all MOFs in Fig. 6. Individual pictures and values for each MOF are given in the supplemental material.

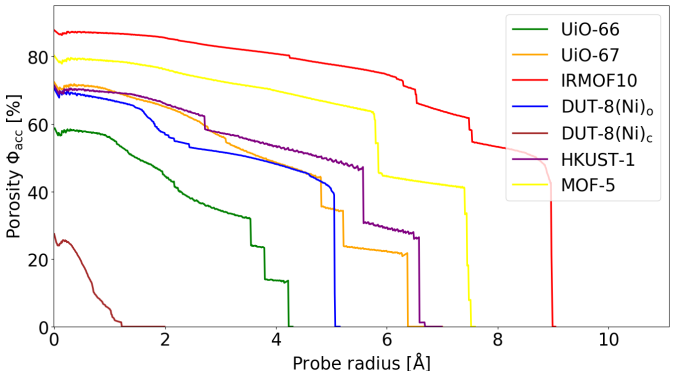

FIG. 6. Probe radius dependence for some MOFs. The accessible porosity is given on the y-axis, while the probe radius is shown on the x-axis. The used grid is approximately 10 points/Å for all MOFs besides UiO-66 (12.5 points/Å) and DUT-8(Ni)$_{\text{closed}}$ (20 points/Å). The drops in the accessible porosity correspond to different pore sizes/radii.

Given the results of Fig. 6, it is obvious that different species have different accessible porosities, because of their different probe radii. For example, compare the effective probe radii of Xe (2.16 Å), CH_4 ($\approx$ 2.29 Å), SO_4^{2-} ($\approx$ 3.01 Å) and C_2H_6 ($\approx$ 5.48 Å). These values were determined by using the bond distances and the vdW radii of the atoms. For C_2H_6, the distance between the most distant H atoms was used. It should be noted that all molecules are approximated as spheres having some effective probe radius, with the goal to make the comparison and the used probe radii more intuitive to understand. This shall not be interpreted as an accurate approximation for, e.g., adsorption investigations (clearly, C_2H_6 is not spherical and shape effects become important), but only as a way to analyze the probe radius dependence.

The accessible porosity for such species will be smaller than for, e.g., H (r_{probe} = 1.20 Å) or He (r_{probe} = 1.40 Å). To illustrate this more quantitatively, the accessible porosities for different probe radii are listed in Tab. II. The same analysis was done with PLATON[14] and Zeo++[18,34–37] (see supplemental material). The general trends for the probe radius dependence for all investigated MOF are consistent between the used codes. As an example, the accessible porosity for UiO-66 behaves as follows: 59.1 % (r_{probe} = 0.00 Å) to 53.3 % (r_{probe} = 1.20 Å) to 50.8 % (r_{probe} = 1.40 Å) to 42.9 % (r_{probe} = 2.16 Å) to 39.9 % (r_{probe} = 2.29 Å) to 34.2 % (r_{probe} = 3.01 Å) to 0.0 % (r_{probe} = 5.48 Å). Furthermore, it should be mentioned that the void porosity is recovered for r_{probe} = 0.00 Å. In addition, the accessible porosity has to become zero for $r_{\text{probe}} \to \infty$.

TABLE II. Accessible porosities (in %) for some MOFs depending on different probe radii (in Å). The used grid contains ca. 10 points/Å, except for UiO-66 where the grid point density is 12.5 points/Å. Values with an * indicate that the smallest pore window (see section IV) in the system is smaller than the probe radius. Thus, the accessible volumes become inaccessible.

r_{probe}	0.00	1.20	1.40	2.16	2.29	3.01	5.48
DUT-8(Ni)$_o$	70.5	66.3	65.6	55.7	54.5	51.7	0.0*
UiO-66	59.1	53.3	50.8	42.9*	39.9*	34.2*	0.0*
UiO-67	72.4	68.8	67.8	64.1	63.2	56.4*	23.2*
IRMOF-10	87.8	86.6	86.5	85.0	84.6	82.8	76.4
MOF-5	80.2	78.3	77.9	75.4	75.0	72.6	64.5*
HKUST-1	71.4	69.1	68.9	65.1*	64.6*	57.3*	47.0*

Besides its fundamental importance, a screening of different probe radii can be performed to analyze the pore sizes of MOFs. One can calculate the porosities for different probe radii, and monitor the corresponding accessible porosity. Once the probe radius is larger than a specific pore, all grid points within this pore become inaccessible. Accordingly, the accessible porosity drops significantly. This gives an intuitive way to characterize the pore sizes (see Fig. 6). More information is given in the supplemental material.

A more accurate approach to analyze the pore dimensions/ pore size distribution is discussed in the next section.

III. PORE SIZE DISTRIBUTION

An approach to determine the pore sizes based on Monte-Carlo (MC) has been implemented. The strategy is straightforward. At first, N random starting points i within the unit cell are initialized, such that

$$\mathbf{r}_i = \alpha \cdot \mathbf{a} + \beta \cdot \mathbf{b} + \gamma \cdot \mathbf{c}. \tag{9}$$

Here, $\alpha, \beta, \gamma \in [0.1, 0.9]$ are random numbers and $\mathbf{a}$, $\mathbf{b}$ and $\mathbf{c}$ are the unit cell vectors. With that, the initial point is somewhere inside the unit cell (maybe even inside an atom). After this initialization, M Monte-Carlo steps are carried out to move these initial points like

$$x_{i+1} = x_i + (2 \cdot \delta - 1) \cdot a_{\text{step}} \tag{10}$$

$$y_{i+1} = y_i + (2 \cdot \epsilon - 1) \cdot a_{\text{step}} \tag{11}$$

$$z_{i+1} = z_i + (2 \cdot \zeta - 1) \cdot a_{\text{step}} \tag{12}$$

for the x, y and z components. The random numbers δ, ϵ and ζ are all $\in [0, 1]$ and a_{step} is the step size. After moving a point, the minimal distance to the vdW surface

$$d_{i+1} = \min_A \left(\sqrt{\Delta_x + \Delta_y + \Delta_z} - r_{\text{vdW},A} \right), \quad (13)$$

$$\text{with } \Delta_x = (x_{i+1} - x_A)^2 \quad (14)$$

$$\Delta_y = (y_{i+1} - y_A)^2 \quad (15)$$

$$\Delta_z = (z_{i+1} - z_A)^2, \quad (16)$$

is computed. Here, $r_{\text{vdW},A}$ is the vdW radius of atom A. Periodic boundary conditions are taken into account. If $d_i < d_{i+1}$, the new point is reset ($\mathbf{r}_{i+1} = \mathbf{r}_i$). On the other hand, if $d_i > d_{i+1}$, the new point is kept ($\mathbf{r}_i = \mathbf{r}_{i+1}$). Then, the next MC step is carried out. With that, d is maximized. This procedure is done for all N initial points until the maximum number of MC steps M is reached. Several initial points ensure that different pores inside MOFs can be analyzed. This gives information about the pore size distribution (PSD), simply by analyzing how many starting points end up in the same pore (i.e., bigger pores have more, smaller pores have less final points).

The step size a_{step} is changed throughout the MC cycle, and adapted to the structure under consideration. As a starting point, the length of the largest cell vector $l_{\text{max}} = \max(|\mathbf{a}|, |\mathbf{b}|, |\mathbf{c}|)$ is taken. The initial step size is defined as $a_{\text{step}}^{\text{init}} = l_{\text{max}}/10$. The step size is adjusted as shown in Tab. III and Fig. 7.

TABLE III. Adaptive step size a_{step} with respect to the MC steps, given in intervals of fractions of the total number of MC steps M.

Fraction of M	$a_{\text{step}}/a_{\text{step}}^{\text{init}}$
[0.00,0.25]	1.000
]0.25,0.50]	0.100
]0.50,0.75]	0.010
]0.75,1.00]	0.001

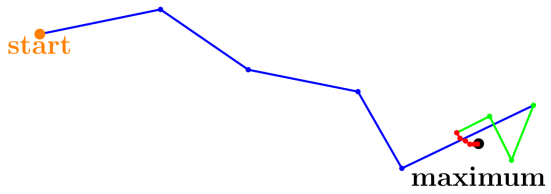

FIG. 7. Illustration of the adaptive step size used in the calculation of the pore size distribution. The black dot is the maximum, while the orange dot indicates the starting point. Three different step sizes are shown for simplicity. Blue indicates the largest step size, green refers to the next smaller step size and red corresponds to the smallest step size. With this scheme, accurate results are obtained using a small number of steps. This is not possible by only using one of these step sizes.

This adaptive way of generating the step size has several advantages over a fixed step size. Given that the step size in the beginning of the MC cycle is fairly large, the steps taken are large, too. With that, the points are moved much more quickly towards a nearby maximum, especially when the starting point is far away from any maximum (e.g., if it was initialized inside an atom). By reducing the step size over the course of the MC cycle, the maximum can be approached more and more accurately without the need for a very large number of MC steps (which would be necessary for a fixed a_{step}). For the last steps, the position of the pore centers as well as the pore diameters are determined very accurately (typically, the final values are within 10^{-3}-10^{-4} Å of the theoretical maximum. This can be checked for structures where the pore centers can be determined by symmetry arguments, like in the UiOs). With this ansatz, only a small number of MC steps (usually about 1000) is needed to properly converge the results. For bigger unit cells one should consider using larger M to avoid having insufficient MC steps to reach a maximum. The PSDs for the considered MOFs are summarized in Tab. IV and Fig. 8.

TABLE IV. Pore sizes distributions, using the pore diameters d_{pore} (in Å) and their distribution Γ (in %), evaluated from the Monte-Carlo procedure described in the text. For the distribution, every pore size with less than 5 % has been disregarded. Accordingly, $\sum_i \Gamma_i$ might not add up to 100 %. For these values, $N = 200$ and $M = 2000$.

MOF	d^1_{pore}	Γ	d^2_{pore}	Γ	d^3_{pore}	Γ
DUT-8(Ni)$_o$	10.18	95.5				
UiO-66	7.19	23.0	7.71	26.5	8.44	50.5
UiO-67	9.63	16.0	10.42	17.5	12.75	66.5
IRMOF-10	18.02	99.5				
MOF-5	11.82	28.0	15.10	72.0		
HKUST-1	5.54	17.0	11.15	46.0	13.37	37.0

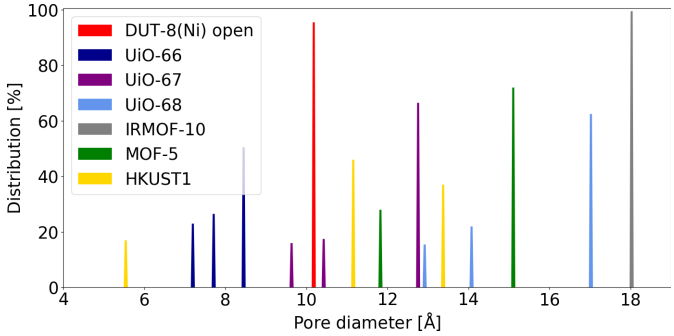

FIG. 8. Pore size distributions (PSDs) for selected MOFs. Using $N = 200$ and $M = 2000$, see text for details.

IV. PORE WINDOWS

For an accurate determination of the porosity, it is important to not only analyze which regions in a MOF are occupied, void or accessible, and how large the pores are. It is also essential to analyze how large the windows between pores are. The pore window is the largest possi-

ble size a species can have to travel through the porous framework. Thus, if the species would theoretically fit into a pore, but cannot reach it due to a smaller pore window, the pore itself has unoccupied volume, which is however inaccessible. To analyze the pore window, the following ansatz is chosen. First, the PSD (see last section) is computed. With that, the centers of all pores within a MOF are known. Then, one draws a line in between all pores (taking periodic boundary conditions into account). The smallest distance of this line to the vdW surface is characterizing a minimum radius r_{min} between two pores. This approach is summarized in Fig. 9 using UiO-66.

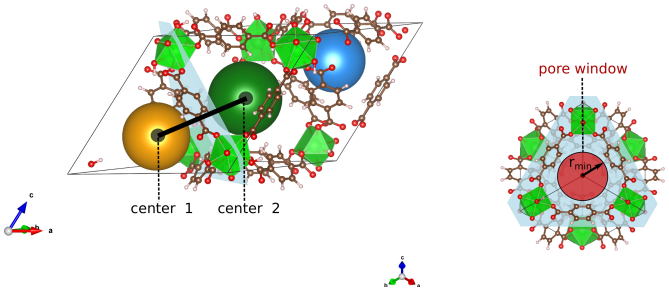

FIG. 9. Visualization of the pore window in UiO-66. The pore window is characterized as the minimal distance to the vdW surface on a line between pore centers. The picture was generated using the VESTA and the INKSCAPE program.

An additional characteristic of a pore window is that it lies in between two pores. With that, if the distance between the coordinate of r_{min} and the pore centers, $\min(d_{\text{center}})$, is very different from the respective pore sizes d_{pore} (i.e., $|\min(d_{\text{center}}) - d_{\text{pore}}|/d_{\text{pore}} > 0.3$), the r_{min} does not represent a pore window. This corresponds to a case where the position of r_{min} lies almost completely within one pore, not between two pores. For example, in UiO-68 one initially finds four r_{min} with 1.89 Å, 2.06 Å, 4.22 Å and 4.69 Å. However, the first two are not pore windows and need to be excluded. Thus, the actual pore windows in UiO-68 are 4.22 Å and 4.69 Å.

By employing this approach, the pore windows for all MOF were evaluated. The smallest one is the limiting pore window. If the probe radius is larger than this limiting pore window, the porosity/volume that is evaluated to be accessible becomes inaccessible. To justify this approach, the calculated pore windows are compared to ZEO++[18,34–37] and PYWINDOW[38]. We find consistent results, which are summarized in Tab. V.

There is only one pore window for DUT-8(Ni)$_{\text{o}}$, IRMOF-10 and MOF-5, but there are two different pore windows in all UiOs and HKUST-1. The smaller one in each MOF represent the limiting pore window.

The presented ansatz is computationally efficient, and only requires an accurate PSD. The PSD only needs to be computed once per structure. Thus, once the PSD is known, the pore windows can be evaluated and analyzed with respect to different used grids.

TABLE V. Pore windows r_{window} (in Å) for the given MOFs, including a comparison to ZEO++[18,34–37] and PYWINDOW[38].

MOF	r_{window} porE: r_1	porE: r_2	ZEO++	PYWINDOW
DUT-8(Ni)$_{\text{o}}$	4.05		4.60	4.80
UiO-66	1.84	2.06	2.06	2.09
UiO-67	2.59	2.91	3.02	3.05
IRMOF-10	5.88		6.09	5.67
MOF-5	3.91		3.96	3.97
HKUST-1	1.84	3.21	3.32	3.33

V. COMPARISON TO REFERENCES

To further validate the implementation in `porE`, several reference calculations were performed. For this, we used the codes RASPA2[16,17], POREBLAZER[15], PLATON[14] and ZEO++[18,34–37].

TABLE VI. Comparison of calculated porosities between reference codes (RASPA2[16,17] (π), POREBLAZER[15] (ρ), PLATON[14] (γ), ZEO++[18,34–37] (ξ)), literature values and the presented approaches (OSA (α) and GPA (ω)). For the GPA, a differentiation between void and accessible porosities (using $r_{\text{probe}} = 1.20$ Å and the largest possible grids) is done. All porosities are given in %. The literature values (REF) are: DUT-8(Ni)[23], UiO-66 and UiO-67[39], IRMOF-10[26], MOF5 and MOF-210[31], HKUST-1[12,40].

MOF	π	ρ	γ	ξ	α	ω_{void}	ω_{acc}	Φ_{REF}
DUT-8(Ni)$_{\text{o}}$	70	68	66	68	61	70	67	67
DUT-8(Ni)$_{\text{c}}$	0	0	0	0	−1	27	1	0
UiO-66	52	51	53	55	49	59	54	53
UiO-67	72	72	69	70	68	72	69	68
IRMOF-10	91	90	86	87	88	88	87	87
MOF-5	81	81	76	79	77	80	79	79
HKUST-1	73	72	69	69	68	71	69	68
MOF-210	93	—	—	88	90	—	—	89

The RASPA2 code provides various features for the calculation of porous materials. The porosity can be accessed using the calculation mode for the determination of the helium void fraction. For that, the porous structure is probed with a helium atom at room temperature. The helium atom itself is described with a TraPPE force field[16,17,41], while the porous structure can be described with various available force fields. For our reference calculations, we used the CrystalGenerator force field[16,17], 2000 Monte Carlo cycles and the unit cell of the MOFs. The used unit cells contain the following amount of atoms: DUT-8(Ni)$_{\text{open}}$ (132), DUT-8(Ni)$_{\text{closed}}$ (66), UiO-66 (114), UiO-67 (174), HKUST-1 (156), IRMOF-10 (166), MOF-5 (424) and MOF-210 (1854). All structures are available at `https://github.com/kaitrepte/porE`. The PLATON code offers several analysis techniques for crystal structures. It allows to analyze the accessible porosity using a grid based approach, similar to the GPA presented here. The POREBLAZER code can

be used to analyze the surface areas, the pore size distribution and the porosity. In POREBLAZER, the porous system is described using the universal force field (UFF[42]) and the helium atoms are describe using a Lennard-Jones force field description. The (helium) void volume is calculated using a cublet procedure. In ZEO++, the accessible volume is calculated by placing points randomly in the unit cell. Afterwards, each point is analyzed regarding its accessibility with respect to a given probe radius using a Voronoi decomposition scheme[18].

In general the void porosities using `porE` with the GPA agree well with the results of the RASPA2 and the PORE-BLAZER code (see Tab. VI). The accessible porosities applying `porE` with the GPA is in excellent agreement with the results calculated with the PLATON and the ZEO++ codes (see Tab. VI). Further, the comparison to literature values shows that literature values are accessible porosities, while the corresponding probe radius is usually not provided. The void porosities do not accurately reflect the porous nature of the MOFs.

This is especially true for systems with more complex pores, where the probe radius plays a crucial role (compare, e.g., UiO-66 and MOF-5). In MOFs with large, open pores the void porosity will already reflect the porous nature of the MOF fairly accurately. If a pore would be entirely spherical, the calculated porosity would be independent of the probe radius (unless $r_{\text{probe}} \geq r_{\text{pore}}$). Using any probe smaller than the pore radius would sample the entire pore, as there are no areas/volumes which are inaccessible. With that, the void and accessible porosities coincide.

However, if the pores are different from the spherical symmetry, e.g., having tetrahedral or octahedral symmetries as in the UiOs, the probe radius dependence becomes significant. In such cases, a sphere is not a suitable approximation for the pores (see Fig. 1 for UiO-66 and UiO-67). Quantitatively, this can be seen for UiO-66 (see table VI), where the void and the accessible porosities are quite different (59 % and 54 % for a probe radius of 1.20 Å). These differences become more pronounced the larger the probe radius becomes. This also explains the rather small dependence of the accessible porosity for $r_{\text{probe}} = 1.20$ Å in IRMOF-10, MOF-5 and HKUST-1 (see table II and the supplemental material), as spheres are a fair approximation to describe the respective pores for these three MOFs.

In summary, the accessible porosities from the GPA are in excellent agreement with literature values, reassuring a proper implementation. Considering its limitations, even the OSA provides reasonable results.

VI. CONCLUSION

We present two approaches to analyze the porosity in porous materials, in specific for metal-organic frameworks (MOFs). Various MOFs (DUT-8(Ni)$_{\text{open}}$, DUT-8(Ni)$_{\text{closed}}$, UiO-66, UiO-67, IRMOF-10, MOF-5, HKUST-1, MOF-210) have been studied using these approaches. One approach is based on overlapping spheres (OSA) and their corresponding volumes, from which the void porosity is calculated. This approach is computationally very efficient. The other approach (GPA) uses a grid within the unit cell. With this approach, a clear differentiation between accessible and void porosities can be made. It was shown that it is essential to converge the results with respect to the used grid. Further, the crucial importance of a clear differentiation between accessible and void porosity for the correct description of porosities in MOFs was demonstrated. For the accessible porosity, it was shown that a correct treatment of the probe radius is essential for reliable results. Thus, this dependence must be considered in any case. In addition, the pore size distribution and the pore windows are analyzed for all MOFs. This is another crucial aspect of an accurate determination of the porosities.

A comparison to reference calculations and literature values confirms that both approaches work as intended, and that the GPA gives very accurate results.

DATA AVAILABILITY

The `porE` code, presented and used within this study, is openly available on GITHUB (`https://github.com/kaitrepte/porE`), and can be referenced via `http://doi.org/10.5281/zenodo.3973264`.

ACKNOWLEDGMENTS

The authors thank the ZIH in Dresden and the HPCC at MSU for computational time and support.

[1] S. Yuan, L. Feng, K. Wang, J. Pang, M. Bosch, C. Lollar, Y. Sun, J. Qin, X. Yang, P. Zhang, Q. Wang, L. Zou, Y. Zhang, L. Zhang, Y. Fang, J. Li, and H.-C. Zhou, "Stable Metal–Organic Frameworks: Design, Synthesis, and Applications," Advanced Materials **30**, 1704303 (2018).

[2] J.-R. Li, R. J. Kuppler, and H.-C. Zhou, "Selective gas adsorption and separation in metal-organic frameworks," Chemical Society Reviews **38**, 1477–1504 (2009).

[3] H. Li, K. Wang, Y. Sun, C. T. Lollar, J. Li, and H.-C. Zhou, "Recent advances in gas storage and separation using metal–organic frameworks," Materials Today **21**, 108 – 121 (2018).

[4] F. X. L. i Xamena, A. Abad, A. Corma, and H. Garcia, "MOFs as catalysts: Activity, reusability and shape-selectivity of a Pd-containing MOF," Journal of Catalysis **250**, 294 – 298 (2007).

[5] L. Jiao, Y. Wang, H.-L. Jiang, and Q. Xu, "Metal–Organic Frameworks as Platforms for Catalytic Applications," Advanced Materials **30**, 1703663 (2018).

[6] F.-L. Li, Q. Shao, X. Huang, and J.-P. Lang, "Nanoscale Trimetallic Metal–Organic Frameworks Enable Efficient Oxygen Evolution Electrocatalysis," Angewandte Chemie International Edition **57**, 1888–1892 (2018).

[7] J. Lei, R. Qian, P. Ling, L. Cui, and H. Ju, "Design and sensing applications of metal–organic framework composites," TrAC Trends in Analytical Chemistry **58**, 71 – 78 (2014), new Nanobiosensing Techniques and Bioanalysis.

[8]Y. Zhang, S. Yuan, G. Day, X. Wang, X. Yang, and H.-C. Zhou, "Luminescent sensors based on metal-organic frameworks," Coordination Chemistry Reviews **354**, 28 – 45 (2018).

[9]S. M. Cohen, "Modifying MOFs: new chemistry, new materials," Chemical Science **1**, 32–36 (2010).

[10]T. D. Bennett and A. K. Cheetham, "Amorphous metal–organic frameworks," Accounts of Chemical Research **47**, 1555–1562 (2014).

[11]S. A. Moggach, T. D. Bennett, and A. K. Cheetham, "The Effect of Pressure on ZIF-8: Increasing Pore Size with Pressure and the Formation of a High-Pressure Phase at 1.47 GPa," Angewandte Chemie International Edition **48**, 7087–7089 (2009).

[12]D. Ongari, P. G. Boyd, S. Barthel, M. Witman, M. Haranczyk, and B. Smit, "Accurate Characterization of the Pore Volume in Microporous Crystalline Materials," Langmuir **33**, 14529–14538 (2017).

[13]A. Bondi, "van der Waals Volumes and Radii," The Journal of Physical Chemistry **68**, 441–451 (1964).

[14]A. L. Spek, "Structure validation in chemical crystallography," Acta Crystallographica Section D **65**, 148–155 (2009).

[15]L. Sarkisov and A. Harrison, "Computational structure characterisation tools in application to ordered and disordered porous materials," Molecular Simulation **37**, 1248–1257 (2011).

[16]D. Dubbeldam, A. Torres-Knoop, and K. S. Walton, "On the inner workings of Monte Carlo codes," Molecular Simulation **39**, 1253–1292 (2013).

[17]D. Dubbeldam, S. Calero, D. E. Ellis, and R. Q. Snurr, "RASPA: molecular simulation software for adsorption and diffusion in flexible nanoporous materials," Molecular Simulation **42**, 81–101 (2016).

[18]T. F. Willems, C. H. Rycroft, M. Kazi, J. C. Meza, and M. Haranczyk, "Algorithms and tools for high-throughput geometry-based analysis of crystalline porous materials," Microporous and Mesoporous Materials **149**, 134–141 (2012).

[19]S. Chavan, J. G. Vitillo, D. Gianolio, O. Zavorotynska, B. Civalleri, S. Jakobsen, M. H. Nilsen, L. Valenzano, C. Lamberti, K. P. Lillerud, and S. Bordiga, "H_2 storage in isostructural UiO-67 and UiO-66 MOFs," Physical Chemistry Chemical Physics **14**, 1614–1626 (2012).

[20]K. Trepte, J. Schaber, S. Schwalbe, F. Drache, I. Senkovska, S. Kaskel, J. Kortus, E. Brunner, and G. Seifert, "The origin of the measured chemical shift of ^{129}Xe in UiO-66 and UiO-67 revealed by DFT investigations," Physical Chemistry Chemical Physics **19**, 10020–10027 (2017).

[21]K. Trepte, S. Schwalbe, J. Schaber, S. Krause, I. Senkovska, S. Kaskel, E. Brunner, J. Kortus, and G. Seifert, "Theoretical and experimental investigations of 129Xe NMR chemical shift isotherms in metal–organic frameworks," Physical Chemistry Chemical Physics **20**, 25039–25043 (2018).

[22]Q. Yang, V. Guillerm, F. Ragon, A. D. Wiersum, P. L. Llewellyn, C. Zhong, T. Devic, C. Serre, and G. Maurin, "CH4 storage and CO2 capture in highly porous zirconium oxide based metal-organic frameworks," Chemical Communications **48**, 9831–9833 (2012).

[23]V. Bon, N. Klein, I. Senkovska, A. Heerwig, J. Getzschmann, D. Wallacher, I. Zizak, M. Brzhezinskaya, U. Mueller, and S. Kaskel, "Exceptional adsorption-induced cluster and network deformation in the flexible metal–organic framework DUT-8(Ni) observed by in situ X-ray diffraction and EXAFS," Physical Chemistry Chemical Physics **17**, 17471–17479 (2015).

[24]K. Trepte, S. Schwalbe, and G. Seifert, "Electronic and magnetic properties of DUT-8(Ni)," Physical Chemistry Chemical Physics **17**, 17122–17129 (2015).

[25]S. Schwalbe, K. Trepte, G. Seifert, and J. Kortus, "Screening for high-spin metal organic frameworks (MOFs): density functional theory study on DUT-8(M1,M2) (with Mi = V,...,Cu)," Physical Chemistry Chemical Physics **18**, 8075–8080 (2016).

[26]M. Eddaoudi, J. Kim, N. Rosi, D. Vodak, J. Wachter, M. O'Keeffe, and O. M. Yaghi, "Systematic Design of Pore Size and Functionality in Isoreticular MOFs and Their Application in Methane Storage," Science **295**, 469–472 (2002).

[27]N. L. Rosi, J. Eckert, M. Eddaoudi, D. T. Vodak, J. Kim, M. O'Keeffe, and O. M. Yaghi, "Hydrogen Storage in Microporous Metal-Organic Frameworks," Science **300**, 1127–1129 (2003).

[28]S. S.-Y. Chui, S. M.-F. Lo, J. P. H. Charmant, A. G. Orpen, and I. D. Williams, "A Chemically Functionalizable Nanoporous Material [Cu3(TMA)2(H2O)3]n," Science **283**, 1148–1150 (1999).

[29]C. H. Hendon and A. Walsh, "Chemical principles underpinning the performance of the metal–organic framework HKUST-1," Chemical Science **6**, 3674–3683 (2015).

[30]K. T. Butler, C. H. Hendon, and A. Walsh, "Electronic Chemical Potentials of Porous Metal–Organic Frameworks," Journal of the American Chemical Society **136**, 2703–2706 (2014).

[31]H. Furukawa, N. Ko, Y. B. Go, N. Aratani, S. B. Choi, E. Choi, A. Ö. Yazaydin, R. Q. Snurr, M. O'Keeffe, J. Kim, and O. M. Yaghi, "Ultrahigh Porosity in Metal-Organic Frameworks," Science **329**, 424–428 (2010).

[32]K. D. Gibson and H. A. Scheraga, "Exact calculation of the volume and surface area of fused hard-sphere molecules with unequal atomic radii," Molecular Physics **62**, 1247–1265 (1987).

[33]R. D. Johnson, *NIST Computational Chemistry Comparison and Benchmark Database* (NIST Standard Reference Database Number 101, 19–04–2018).

[34]R. L. Martin, B. Smit, and M. Haranczyk, "Addressing Challenges of Identifying Geometrically Diverse Sets of Crystalline Porous Materials," Journal of Chemical Information and Modeling **52**, 308–318 (2012).

[35]M. Pinheiro, R. L. Martin, C. H. Rycroft, A. Jones, E. Iglesia, and M. Haranczyk, "Characterization and comparison of pore landscapes in crystalline porous materials," Journal of Molecular Graphics and Modelling **44**, 208 – 219 (2013).

[36]M. Pinheiro, R. L. Martin, C. H. Rycroft, and M. Haranczyk, "High accuracy geometric analysis of crystalline porous materials," CrystEngComm **15**, 7531–7538 (2013).

[37]R. L. Martin and M. Haranczyk, "Construction and Characterization of Structure Models of Crystalline Porous Polymers," Crystal Growth & Design **14**, 2431–2440 (2014).

[38]M. Miklitz and K. E. Jelfs, "pywindow: Automated Structural Analysis of Molecular Pores," Journal of Chemical Information and Modeling **58**, 2387–2391 (2018).

[39]H. Wu, T. Yildrim, and W. Zhou, "Execptional Mechanical Stability of Highly Pourous Zirconium Metal-Organic Framework UiO-66 and Its Important Implications," The Journal of Physical Chemistry Letters **4**, 925–930 (2013).

[40]J. A. Mason, M. Veenstra, and J. R. Long, "Evaluating metal–organic frameworks for natural gas storage," Chemical Science **5**, 32–51 (2014).

[41]M. G. Martin and J. I. Siepmann, "Transferable potentials for phase equilibria. 1. United-atom description of n-alkanes," The Journal of Physical Chemistry B **102**, 2569–2577 (1998).

[42]A. K. Rappe, C. J. Casewit, K. S. Colwell, W. A. Goddard, and W. M. Skiff, "UFF, a full periodic table force field for molecular mechanics and molecular dynamics simulations," Journal of the American Chemical Society **114**, 10024–10035 (1992).